

Vesiculation of high fountaining Hawaiian eruptions: episodes 15 and 16 of 1959 Kīlauea Iki

Wendy K. Stovall · Bruce F. Houghton ·
Julia E. Hammer · Sarah A. Fagents · Don A. Swanson

Received: 27 November 2010 / Accepted: 6 August 2011 / Published online: 27 September 2011
© Springer-Verlag (outside the USA) 2011

Abstract The 1959 summit eruption of Kīlauea volcano produced the highest recorded Hawaiian fountain in Hawai‘i. Quantitative analysis of closely spaced samples from the final two high-fountaining episodes of the eruption result in a fine-scale textural study of pyroclasts and provide a record of postfragmentation processes. As clast vesicularity increases, the vesicle number density decreases and vesicle morphology shifts from small and round to larger and more irregular. The shift in microtexture corresponds to greater degrees of postfragmentation expansion of clasts with higher vesicularity. We suggest the range of clast morphologies in the deposit is related to thermal zonation within a Hawaiian fountain where the highest vesicularity clasts traveled in the center and lowest traveled

along the margins. Vesicle number densities are greatest in the highest fountaining episode and therefore scale with intensity of activity. Major element chemical analyses and fasciculate crystal textures indicate microlite-rich zones within individual clasts are portions of recycled lava lake material that were incorporated into newly vesiculating primary melt.

Keywords Vesiculation · Hawaiian eruptions · Kīlauea Iki · Fasciculate crystal texture · Lava lake

Introduction

High-fountaining Hawaiian eruptions

Hawaiian eruptions produce incandescent fountains of molten pyroclastic material that can reach hundreds of meters in height. They occur at basaltic volcanoes such as Etna in Italy (Polacci et al. 2006; Andronico et al. 2008; Bertagnini et al. 1989) and Kīlauea in Hawai‘i (Heliker and Mattox 2003; Richter et al. 1970; Swanson et al. 1979). Fountaining eruptions typically begin as fissure-fed discharges, focusing with time on one or more point sources, increasing in intensity over several cycles, and reaching maximum discharge and fountain height later in the eruption. Early activity in the 1983–1986 Pu‘u ‘Ō‘ō eruption of Kīlauea, Hawai‘i produced average fountain heights of ~170 m in the first 23 episodes before eruption rates increased and fountains consistently reached >400 m high (470 m maximum) until the 39th episode (Heliker and Mattox 2003). Similar activity occurred in 1969 during the first 6 months of the Mauna Ulu eruption, Kīlauea, Hawai‘i. Relatively low initial fountaining episodes increased to 540 m height in the ninth episode (Swanson et al. 1979).

Editorial responsibility: B. van Wyk de Vries

W. K. Stovall · B. F. Houghton · J. E. Hammer
Department of Geology and Geophysics,
University of Hawai‘i at Mānoa,
1680 East-West Road,
Honolulu, HI 98622, USA

S. A. Fagents
Hawai‘i Institute of Geophysics and Planetology,
University of Hawai‘i at Mānoa,
1680 East-West Road,
Honolulu, HI 98622, USA

D. A. Swanson
US Geological Survey, Hawaiian Volcano Observatory,
P.O. Box 51, Hawai‘i National Park,
Hawaii, HI 96718, USA

Present Address:

W. K. Stovall (✉)
US Geological Survey, Volcano Science Center,
345 Middlefield Road MS 910,
Menlo Park, CA 94025, USA
e-mail: wstovall@usgs.gov

The eruption of Kīlauea Iki in 1959 also started from a fissure and displayed low fountaining before producing the highest fountain ever recorded at Kīlauea (580 m) during the 15th of 17 episodes (Richter et al. 1970). At Etna, lava fountaining activity ranges from sustained episodes (e.g., Alparone et al. 2003) to discrete, outbursts (e.g., Andronico et al. 2008) with fountain heights up to 800 m (Alparone et al. 2003). The commonality among individual episodes of activity at all of these volcanoes is that lava fountaining ceased abruptly with little waning activity.

Kīlauea Iki 1959 eruption

The 1959 eruption of Kīlauea Iki (Fig. 1) began on November 14 and lasted 36 days (Fig. 2). A steep-sided cone and a tephra blanket were deposited southwest (downwind) of the main vent. Because the vent was on the wall of an existing collapse crater, effusive products of the eruption formed a $\sim 37 \times 10^6 \text{ m}^3$ crater-filling lava lake. Each episode filled the lake to the point where it flowed back into the vent. Typically, low fountaining began each episode and then the intensity increased to produce a higher and more powerful fountain. Fountaining ceased soon after the lake reached the level of the vent and lava immediately poured back down the vent into the conduit system to reach the magma storage region beneath Kīlauea's summit (Eaton et al. 1987). Throughout the course of the eruption,

episodes became shorter and typically more closely spaced in time. The last two significant episodes, 15 and 16 (Fig. 3), were among the three highest of the entire eruption (Fig. 2).

Purpose

This paper examines the vesiculation history of melt erupted in very high-fountaining Hawaiian eruptions, using episodes 15 and 16 as case studies. A secondary aim is to determine what effect, if any, melt draining back from the lava lake into the conduit had on fountain and eruptive behavior. This study also compares these later episodes with the opening episode of the Kīlauea Iki eruption (Stovall et al. 2011) in order to understand why some episodes reach exceptional fountaining heights and others do not, and what factors lead to the termination of Hawaiian fountaining episodes.

Background and previous work

Chronology of episodes 15 and 16

Richter et al. (1970) give a detailed account of the events of the 1959 eruption and is the basis for the following summary of episodes 15 and 16. The 15th episode lasted for slightly more than 4 h beginning at 11:10 AM

Fig. 1 Location map of Kīlauea Caldera and episode 15 and 16 study site. **a** Kīlauea Caldera and Kīlauea Iki crater with whole-deposit tephra isopachs (thickness in cm, Houghton, unpublished data, 2008), Pu'u Pua'i cone summit (C), and study site (X). **b** Island of Hawai'i with *star* marking location of Kīlauea

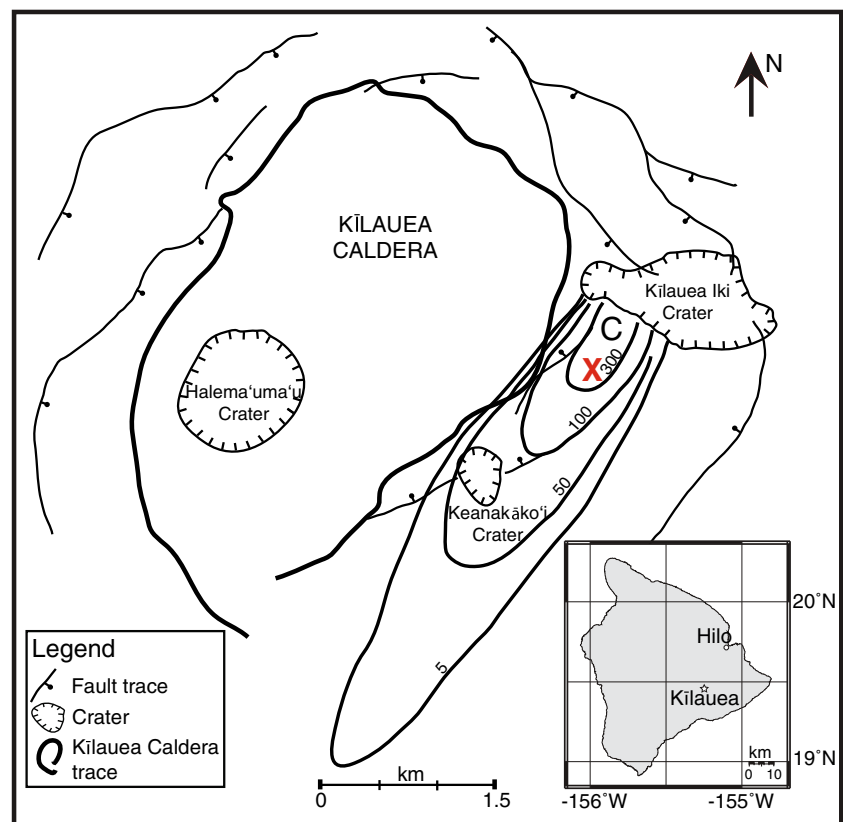
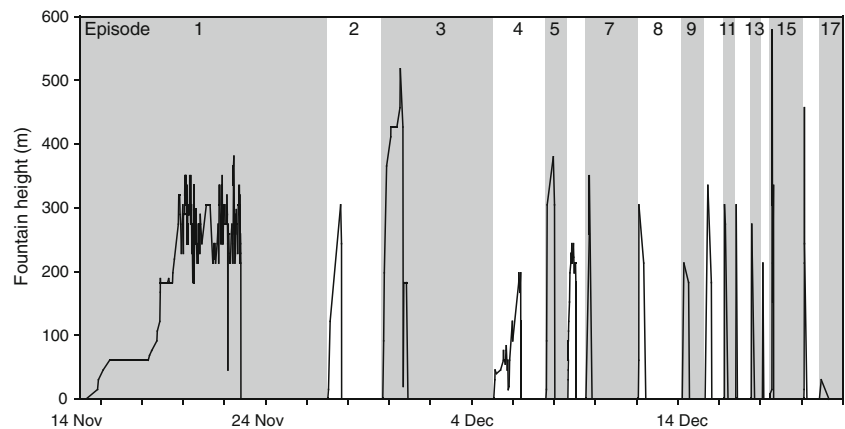


Fig. 2 Kīlauea Iki eruption fountain height. The *numbers* along the top and *shaded stripes* indicate individual episodes



December 17, 1959 with low fountaining (Fig. 3a). During the first 2 h, small fountains 8–15 m high erupted while a lava stream drained from the lake into the vent. Just before 2 PM, activity increased and within 12 min the fountain reached ~580 m (Fig. 3b, c), the highest of the eruption. Activity was sustained at this peak for only a few minutes before fountain heights decreased to ~220 m, where they remained for ~30 min. Then the fountain surged to ~330 m for ~45 min. In the final minute of fountaining, lake lava began to drain into the vent. Hawaiian fountaining activity ceased rather abruptly at 3:32 PM while lava continued to pour into the vent from the lake. Drainback continued throughout the day on December 18 with decreasing flux, and during draining, occasional non-eruptive splashing was observed at the vent.

On December 19 at 2:40 AM, after a 35-h pause in fountaining, the 16th and last high-fountaining episode of the Kīlauea Iki eruption began. The 16th explosive phase started similarly to the 15th phase, but the early low spattering lasted only 20 min before the fountain height increased over 25 min to a height of ~460 m. While the fountain reached and maintained this great height for several minutes, lava also surged into the lake from the base of the fountain. The remaining 170 min of explosive activity were limited to weaker fountains no more than 240 m high (Fig. 3d). At 6:16 AM on the same day, fountaining ceased abruptly and drainback of lake lava into the vent began immediately as a ~60 m-wide funnel-like flow encircling the vent.

Significance of episodes 15 and 16

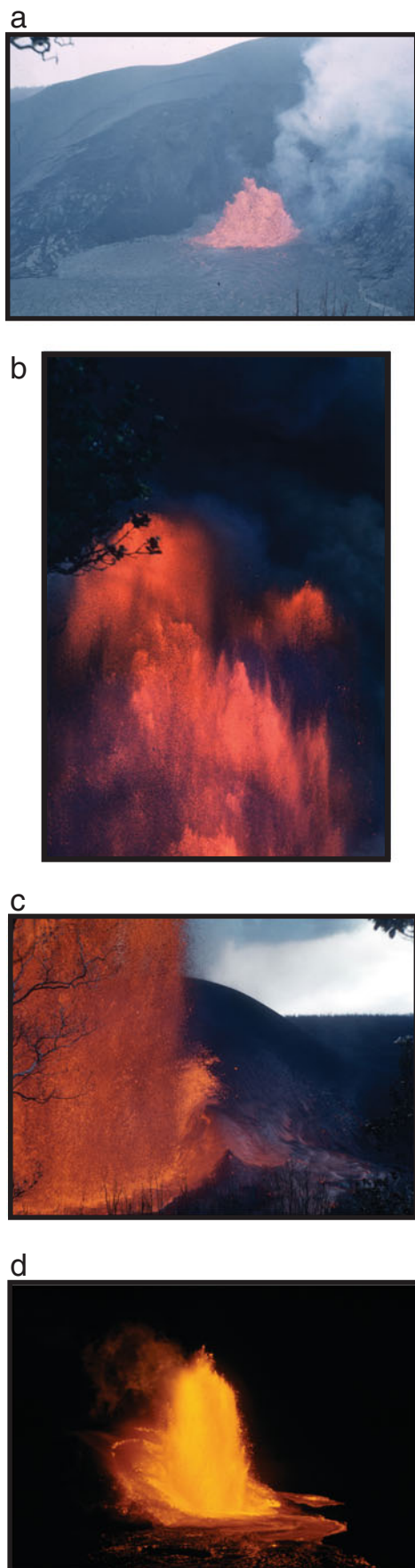
Unlike the first episode of the eruption (Richter et al. 1970; Stovall et al. 2011), fountaining at the start of later episodes cleared the conduit of any relatively outgassed lava that drained back into the vent at the close of the previous episode. Episode 15 produced the highest fountain at ~580 m (Fig. 3b) and this was the episode preceded by the smallest volume of drainback lava (1.0 million m³),

over 7 h 8 min. Episode 16 produced a ~460 m-high fountain and was preceded by 3.2 million m³ of drainback lava over 26 h after the end of episode 15. The coupling of such high-fountaining activity with variable quantities of recycled, drained-back lava make the later episodes of the Kīlauea Iki eruption, and especially these short-lived high-fountain producing episodes, an intriguing case study for mechanisms driving Hawaiian fountaining eruptions.

Techniques

All methodologies associated with sample collection and analysis are consistent with the study of the first episode of the Kīlauea Iki eruption (Stovall et al. 2011). Samples of episodes 15 and 16 tephra were collected at ~5 cm intervals through the entire ~80 cm deposit at the reference site (Fig. 4a). Samples were field-sieved to select at least 100 clasts in the 16–32 mm size fraction (Houghton and Wilson 1989), which were dried in an oven at 112°C for 24 h to remove water. In addition, we analyzed the glass matrix of clasts following the discovery of heterogeneous zones of contrasting vesiculation and color within single clasts.

Samples ρ01, ρ03, ρ05, ρ07, and ρ09 (Fig. 4) were chosen for quantitative analysis of vesicle and crystal populations. This selection includes coarse-grained samples from the peak of each episode and those deposited at the end of each episode. Polished thin sections were made of clasts from the mode and extremes of the density distributions for these samples to ensure capture and quantification of the full vesicularity range of the ejecta. For only clasts with homogeneous textures, nested images were captured with three magnifications: scan using 1,200 dpi on an HP flatbed scanner and 25× and 100× backscatter images on a JEOL-5900LV SEM operating at 15 kV and 1 nA beam current. Image processing and quantitative vesicle analyses were conducted using the methods outlined in Shea et al. (2009).



◀ **Fig. 3** Photographs of Kilauea Iki fountain during episodes 15 and 16 (photos by J. Eaton from the HVO library archives). **a** Lava fountain at the start of episode 15, ~30 m high. **b** Top of episode 15, ~580-m high fountain. **c** Lower portion of ~580-m high fountain and cone with rheomorphic lava flows on cone flank. **d** Episode 16, ~240-m high fountain

Clast morphologies

Componentry of the juvenile clasts was conducted in the laboratory and six morphological classes defined, but not every type was found in every sample (Fig. 5a). *Pumice*, *fluidal*, and *transitional* textures (Fig. 5b, d and c, respectively) are as defined for the 1959 episode 1 tephra (Stovall et al. 2011). Clasts labeled T_O contain domains of reddish oxidized material (Fig. 5e). Clasts labeled T_B are transitional clasts with a bread-crust exterior surface. Large spatter bombs (i.e., the maximum-sized clasts) always fall into this category and are typically either cow dung or ribbon bombs (Fig. 5f, g). These bread crust bombs have interiors with vesicles up to 10 cm diameter.

Electron microprobe analysis

To quantify and compare major-element chemistry within individual zones or domains in heterogeneous clasts (Fig. 6), electron microprobe analysis was conducted on the JEOL JXA-8500F Field Emission Hyperprobe at the University of Hawai'i at Mānoa. Measurements were taken using a 15 kV and 10 nA with a 10 μm defocused beam to ensure minimal Na loss. Total counting times for each element were: Na=20 s, Si=30 s, Ti=20 s, Al=30 s, Fe=15 s, Mn=20 s, Mg=40 s, Ca=30 s, K=30 s, P=30 s, and S=30 s. Backgrounds were measured on both sides of the peak, each at half the counting time of the peak.

Results

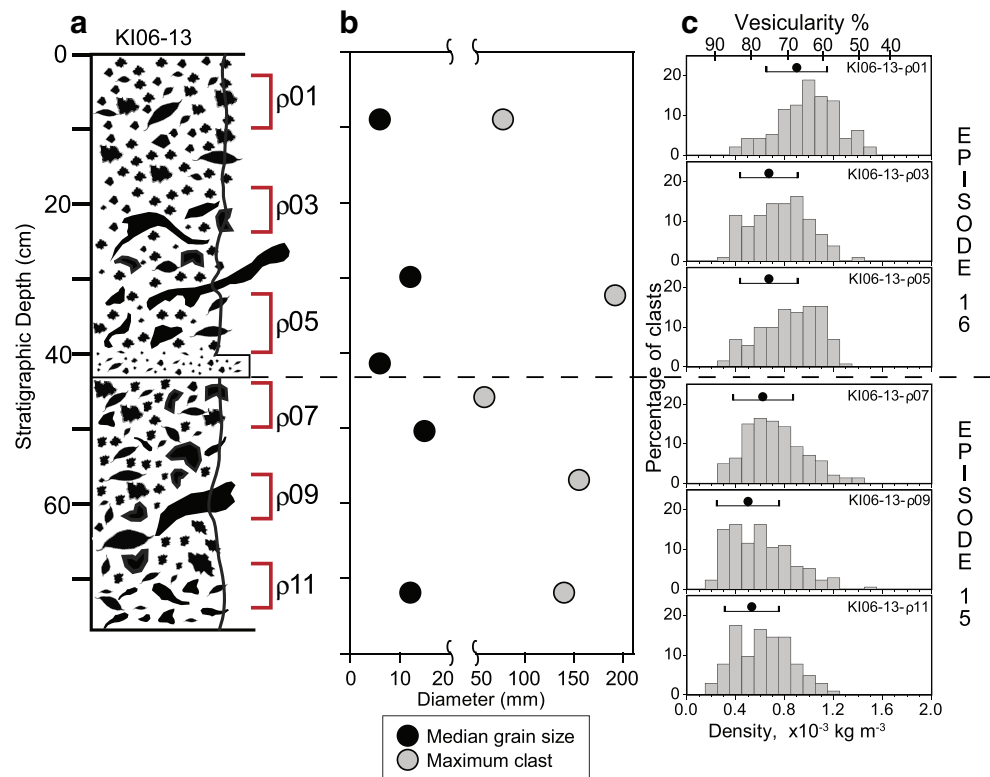
Deposit characteristics

Stratigraphy

The Kilauea Iki tephra stratigraphy has been logged in numerous pits that extend up to 5 km downwind of the Pu'u Pua'i cone (Fig. 1). Existing collapse pits provide sections through the upper ~1 to 2 m of the deposit and expose stratigraphy that is reconcilable at multiple locations. The tephra stratigraphy exposed in the upper pit walls must be associated with the last high-fountaining episodes (Fig. 2).

Figure 4 includes the stratigraphy with sample positions, grain size and maximum clast data, and selected density

Fig. 4 Kīlauea Iki episodes 15 and 16; **a** stratigraphy with sample locations, **b** median grain size and maximum clast diameter, and **c** density distributions for samples taken from locations labeled in stratigraphy. The *dots* above histograms indicate mean density, and *bars* = 1 SD. Maximum clast diameters are calculated from the average of three axes for each of the five clasts



distributions for the upper ~80 cm of a pit 685 m from the vent (Fig. 1). The pit was chosen because it is located along the dispersal axis for episodes 15 and 16 fountaining and because tephra in this location is relatively proximal and yet not welded (as it is within ~450 m of the vent along the axis). In the upper ~80 cm of tephra (Fig. 4a), two distinctive normally graded sequences are separated by a ~3–4 cm markedly finer-grained layer rich in achneliths (Walker and Croasdale 1972) with a sharp lower contact and weakly gradational upper contact. The uppermost 40 cm package contains minor fine ash and grades downward from predominantly 3 mm to 4 cm diameter golden to light brown, highly vesicular clasts to greater proportions of black shiny clasts, and vesicular spatter 5 mm to 8 cm in diameter. Between 20 and 40 cm from the top, large spatter clasts reach up to a maximum of 25 cm in diameter and are flattened or elongate, whereas smaller spatter clasts are equant. The fine-grained achnelith-rich layer at 40–43 cm (Fig. 4a) contains clasts between 3 mm and 2 cm diameter but lacks fine ash. The second graded sequence extends from 43 cm from the top to ~78 cm depth and is similar to the upper one, except that the largest spatter clasts in the lower portion of the sequence reach only 20 cm diameter. The lower contact of this graded sequence is marked by disappearance of large spatter and appearance of a zone dominated by pumice. Based on investigations in multiple pits, the similarity of the two sequences and the achnelith parting between them, we infer

that the upper-graded sequence, including the achnelith-rich layer, was deposited during episode 16 and the lower-graded sequence is the product of episode 15 fountaining (Fig. 4).

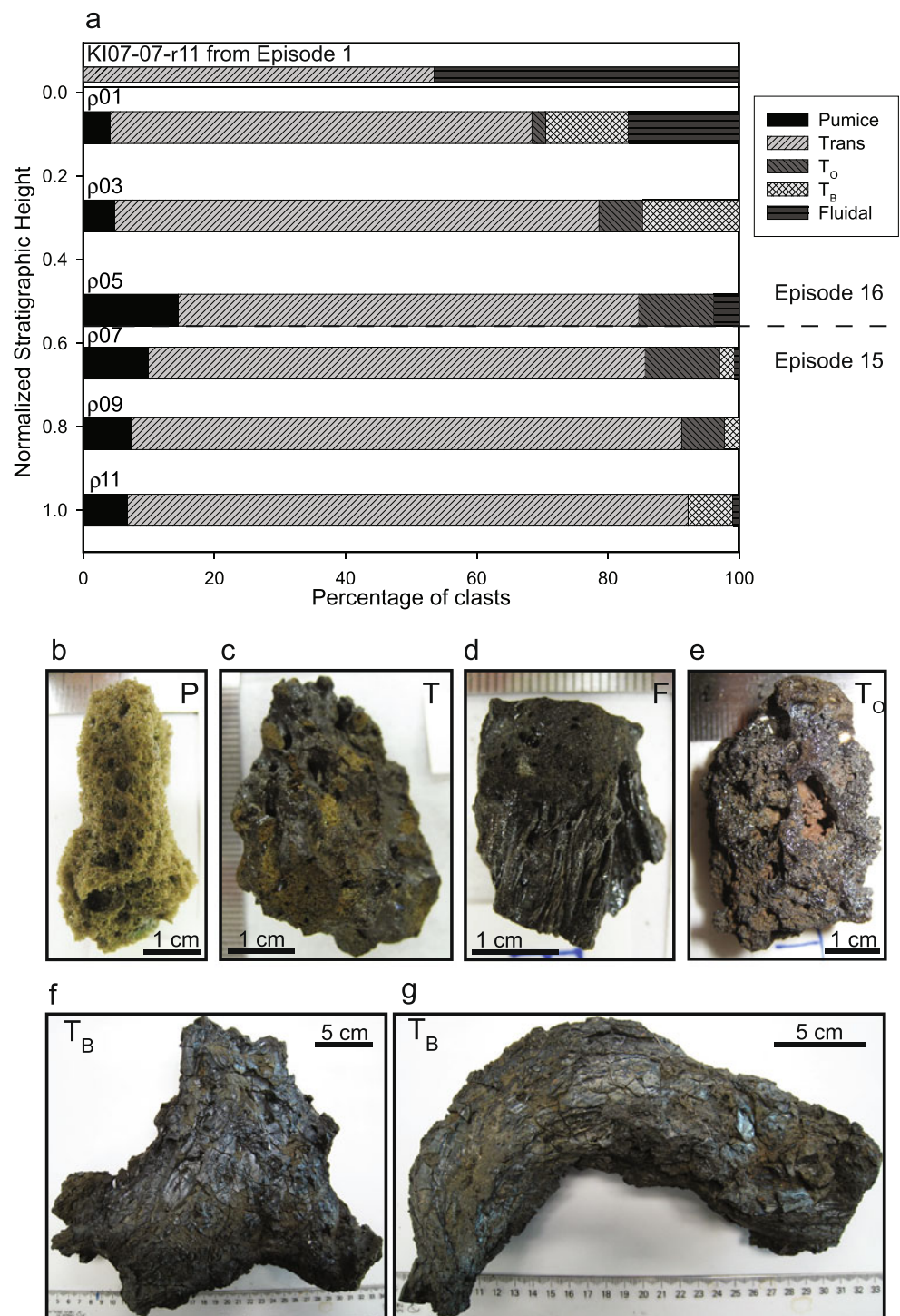
Grain size

Five bulk grain size samples were collected, sieved, and measured prior to this study. The median grain size (Fig. 4b) of the samples ranges between -2.6 and -3.9ϕ (6–15 mm). At five stratigraphic levels, the three dimensions of the five largest clasts were measured and averaged to yield the mean–maximum clast size (Fig. 4b). Maximum clast diameters within the upper portion of each normally-graded sequence are about 60–80 mm, whereas the lower portion of each sequence contains much larger clasts between ~150 and 200 mm in diameter.

Density, bulk vesicularity, and componentry

The range of clast density measurements from episodes 15 and 16 is broad and varies by $1,000$ – $1,200 \text{ kg m}^{-3}$ for every sample (Fig. 4c). The least dense clasts, with highest vesicularity, can be classified as pumice, and the most dense clasts as T_O (oxidized transitional) or fluidal. Transitional clasts span an overlapping and intermediate range of vesicularity from ~90% to ~55%; in samples ρ03, ρ05, and ρ09, there are few fluidal clasts and transitional

Fig. 5 Componentry and clast photographs for episode 15 and 16 samples. **a** Juvenile clast componentry for episodes 15 and 16 Kīlauea Iki tephra; clasts correspond to labeled stratigraphic position in Fig. 4. Top bar is from episode 1 to assist comparison between eruptive episodes. Clast-types with 1 cm bar for scale: **b** pumice P, **c** transitional T, **d** fluidal F, **e** oxidized transitional T_O (**f** and **g**) transitional breadcrust bombs T_B . Componentry data are derived from processing samples of at least 100 clasts of diameter 16–32 mm

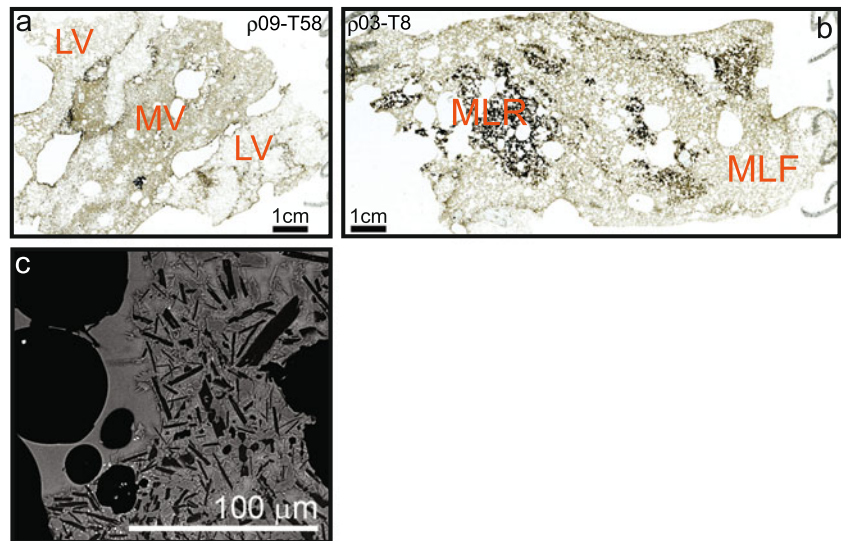


clasts are the least vesicular (densest) clasts used for quantitative microtextural analysis.

Density distributions for episode 15 samples (ρ_{11} , ρ_{09} , and ρ_{07} ; Fig. 3c) are all similar with broad peaks and mean densities of $500\text{--}620\text{ kg m}^{-3}$ (82–78% vesicularity). Sample ρ_{07} , erupted at the end of episode 15, has the greatest diversity of clast types (Fig. 5a) as well as the highest mean density (Fig. 4c).

Episode 16 samples (ρ_{05} , ρ_{03} , and ρ_{01} ; Fig. 4c) have distributions shifted toward higher densities than those of episode 15. The range of mean densities, $670\text{--}900\text{ kg m}^{-3}$, corresponds to 76–68% vesicularity. The densest clasts in this study are in sample ρ_{01} , deposited during the last high fountain of the eruption. It is the only sample from either episode containing all six clast morphologies and has the greatest abundance of fluidal clasts (Fig. 4a).

Fig. 6 Thin section scans for heterogeneous clasts with **a** zones of variable vesicularity and **b** dark, microlite-rich zones within light, microlite-free glass. Standard microprobe images showing **c** fasciculate microlite textures



Qualitative microtexture observations

There are no significant qualitative microtextural differences between clasts from episode 15 (Fig. 7) and episode 16 (Fig. 8). Vesicles are mostly round and variably sized between 5 μm and a few centimeters diameter and the largest

vesicles are the most irregularly shaped (e.g., Fig. 7d, 8d). Olivine phenocrysts are present in all except the most vesicular clasts and their abundance seems unrelated to vesicle number or size distribution (Fig. 7 and 8). On fresh surfaces, most moderately to highly vesicular clasts have a thin vesicle-poor rim (Fig. 7d and 8g). Homogeneous clasts

Fig. 7 Grayscale processed images for homogeneous episode 15 clasts. **a–c** Low-vesicularity, fluidal clast, **d–f** intermediate-vesicularity transitional clast, and **g–i** high-vesicularity, pumice clast. Thin section scans in the top row, SEM ×25 magnification images in second row, SEM ×100 magnification images in third row. Vesicles are *black*, glass is *white*, and crystals are *gray*

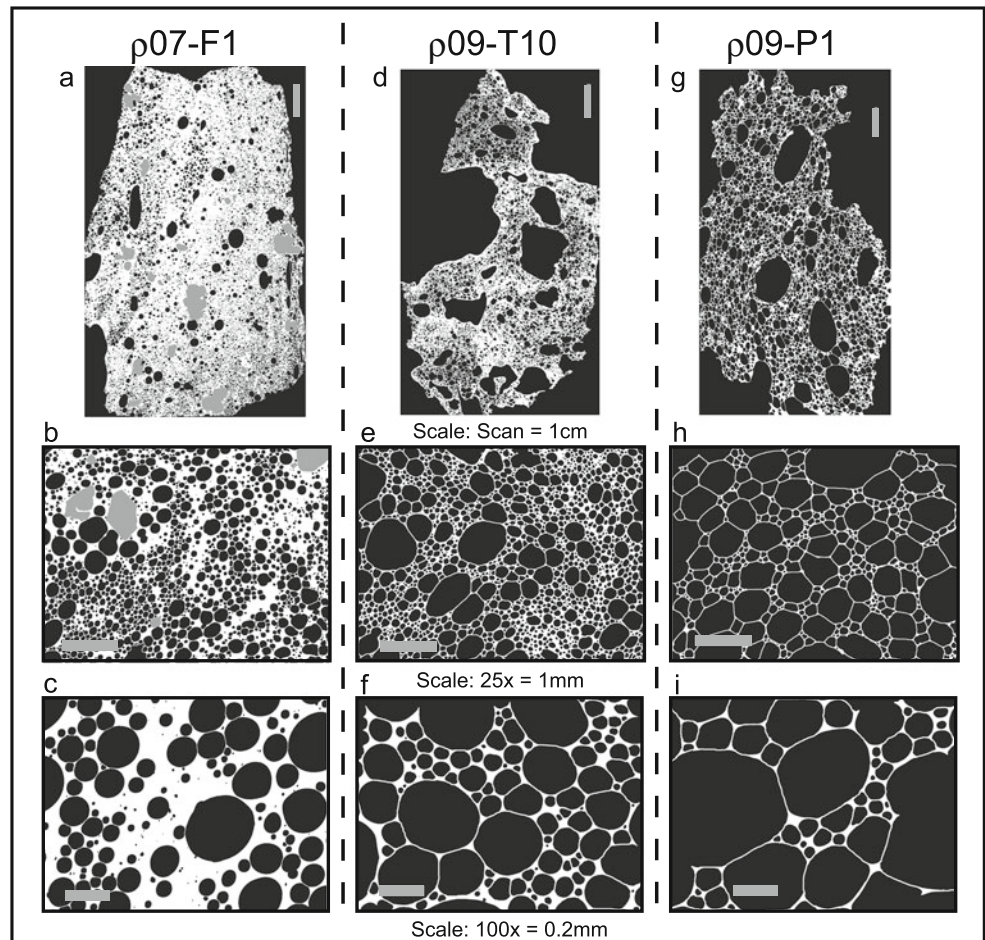
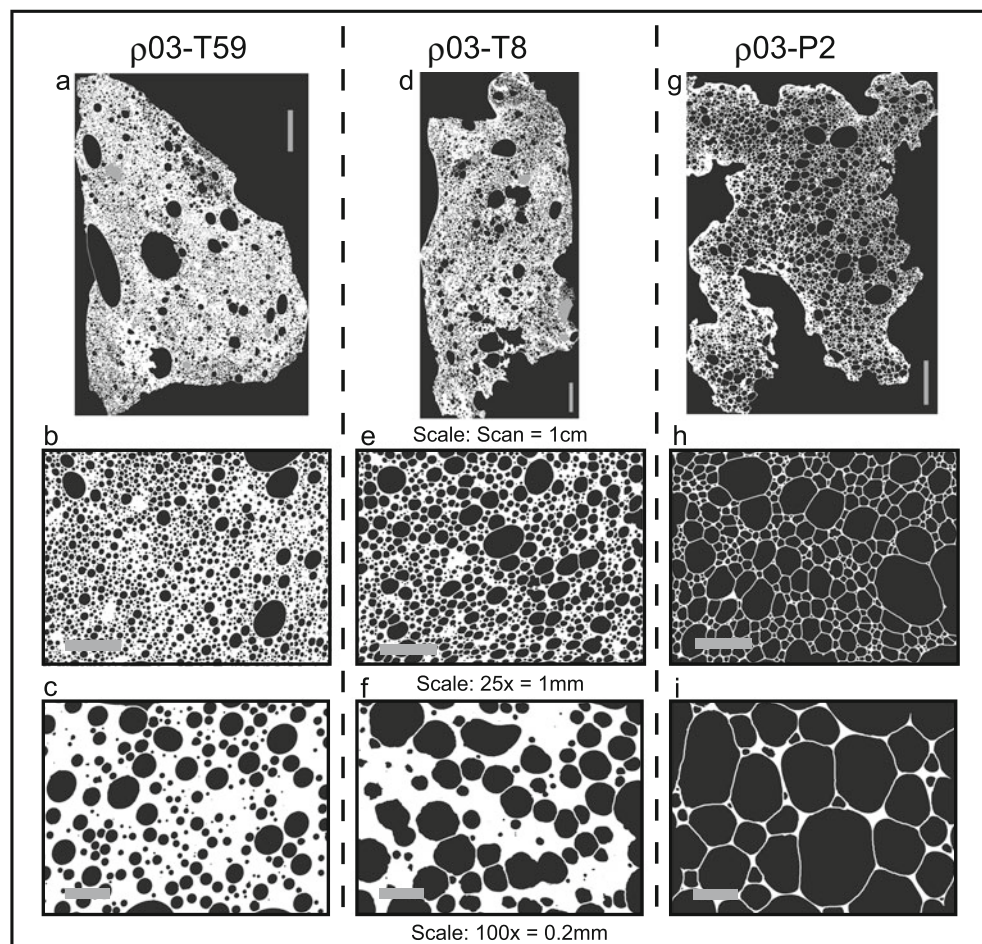


Fig. 8 Grayscale processed images for homogeneous episode 16 clasts. **a–c** Low-vesicularity, transitional clast, **d–f** intermediate-vesicularity transitional clast, and **g–i** high-vesicularity, golden-pumice clast. Thin section scans in the top row, SEM $\times 25$ magnification images in second row, SEM $\times 100$ magnification images in third row. Vesicles are *black*, glass is *white*, and phenocrysts are *gray*



contain even distributions of vesicles with a diversity of sizes (Fig. 7a and 8a) separated by glass walls that thin with increasing vesicularity (e.g., horizontal transition in Fig. 7b, e, h and 8b, e, h). The least vesicular clasts (Fig. 7a–c and 8a–c) contain round vesicles separated by relatively thick walls. Highest-vesicularity pumice clasts (Fig. 7g–i and 8g–i) have foam-like textures, with micron-thick vesicle walls that are flattened against nearest neighbors (e.g., Mangan and Cashman 1996).

Heterogeneous clasts come in two varieties characterized by either (1) mingled more-vesicular (*MV*) and less-vesicular (*LV*) zones (Fig. 6a) or (2) sharply delineated, opaque microlite-rich (*MLR*) zones within golden, translucent microlite-free (*MLF*) glass (Fig. 6b). In the former (Fig. 6a), the *MV* regions have thinner walls and more amoeboid vesicles. *LV* regions contain larger numbers of smaller round vesicles. In *MLF* versus *MLR* zones, vesicle abundance and size are often approximately the same; within the microlite-rich zones, however, there are more amoeboid vesicles. Also within *MLR* regions, vesicle walls are less smooth and appear slightly irregular (Fig. 8f) in comparison to vesicle walls in *MLF* glass (Fig. 7c and 8c).

There are two distinct types of microlite textures, thin stringers and intergrown, fasciculate patches (Fig. 6c).

Stringers are elongate 30–100 μm wide bands of pyroxene microlites that appear most commonly in transitional to fluidal clasts. The edges are sharp and defined by prismatic terminations of radiating spherulites or dendrites that originate at the centerline of the stringer. They sometimes separate *MV* and *LV* zones but are also located within otherwise uniformly vesicular clasts. *MLR* zones contain clusters of microlites with fasciculate (Fig. 6c) texture comprised of intergrown plagioclase and pyroxene crystals that range in length from 0.1 to 0.4 mm. The *MLR* regions are ~ 1 to 15 mm in diameter and the crystal morphology at the boundary of *MLF* glass is similar to the point-centered radiating pyroxene dendrites of the stringers. At the *MLR* zone boundaries, there are occasionally rounded lobes of slightly darker golden glass that protrude into the adjacent, lighter golden *MLF* zone.

Quantitative microtexture observations

Quantitative microtextural analysis of episodes 15 and 16 tephra adds to the study of Kīlauea Iki's opening episode (Stovall et al. 2011) and gives further insight into processes occurring in Hawaiian eruptions. Vesicle volume distributions (*VVDs*) for homogeneous clasts

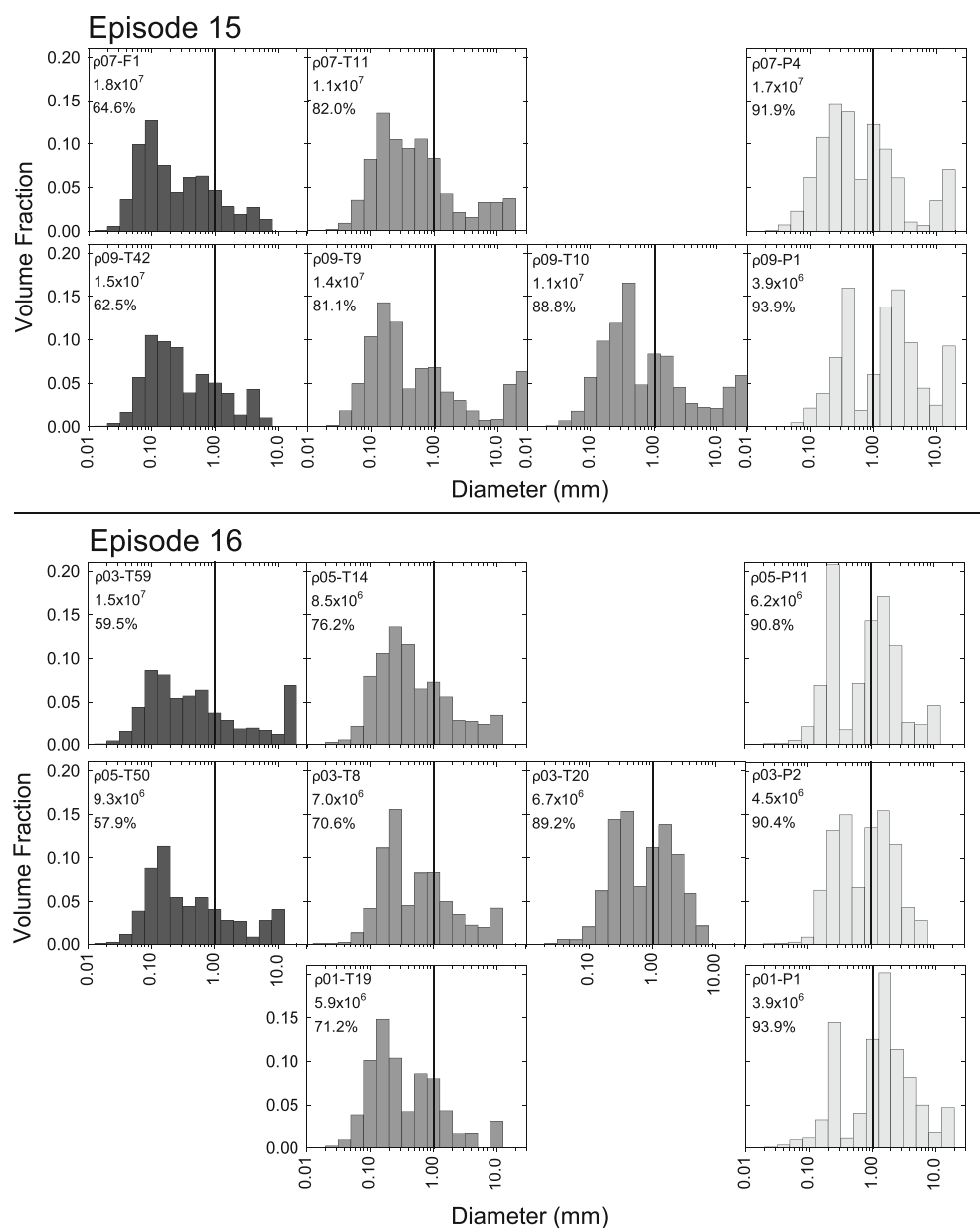
(Fig. 9) are organized according to trends in gas to melt ratio (V_G/V_L ; after Gardner et al. 1996) and changes in the number density (VND), i.e., number of vesicles per unit volume of melt, N_{Vtot}^m (Fig. 10, Table 1). Clasts with vesicularity <75% contain significant numbers of vesicles with equivalent diameter smaller than 10 μm (Fig. 11). These small vesicles account for only minor volume fractions and, therefore, do not appear on VVD plots in Fig. 9.

VVDs for all clasts are bi- to trimodal. Low V_G/V_L clasts ($\rho03\text{--T59}$, $\rho07\text{--F1}$, and $\rho09\text{--T42}$) have the smallest modal diameters (0.1 mm, left column in Fig. 9) and also contain the largest N_{Vtot}^m (Fig. 10). In general, as vesicularity and therefore V_G/V_L increase, the smallest diameter volume

peak coarsens in size and the second mode near 1.0 mm increases in volume. Additionally, increasing vesicularity results in generally larger vesicles (Fig. 11) and a dominant second mode between 1.0 and 2.5 mm (right column P-clasts; Fig. 9).

Episode 15 clasts have generally higher vesicle number densities (Table 1) and span a wider vesicle size range (Fig. 9) than do episode 16 clasts. For this highest-fountaining episode, number densities (N_{Vtot}) are 2.4×10^5 to $6.4 \times 10^6 \text{ cm}^{-3}$ with melt referenced values (N_{Vtot}^m) between 3.9×10^6 and $1.8 \times 10^7 \text{ cm}^{-3}$. In comparison to other basaltic explosive volcanism (Table 1), vesicle number densities for episode 15 are higher than those of the 1983–1986 Pu‘u ‘Ö‘ö tephra (Mangan and Cashman

Fig. 9 Vesicle volume distributions for homogeneous episode 15 and 16 clasts. Distributions of volume fraction of vesicles within a specific size range (VVD) arranged according to vesicle number density (N_{Vtot}^m) and vesicle to melt ratio (V_G/V_L ; see also Fig. 10). Sample number, vesicularity, and vesicle number density per cubic centimeter are included with each histogram (also found in Table 1). Dark to light gray shading corresponds with vesicularity grouping. Vertical lines are drawn at 1.0 mm vesicle diameter to assist comparison



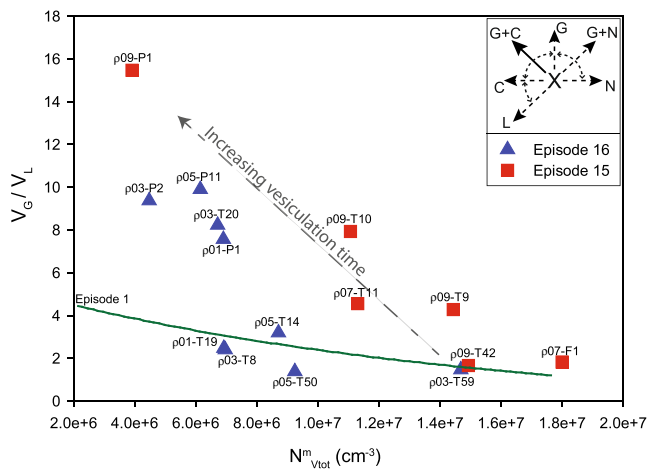


Fig. 10 Volume ratio of vesicles to melt versus vesicle number density ($N_{V_{tot}}^m$) for episode 15 and 16 clasts. Data points are labels of clast name and green line represents trend of data for episode 1 clasts. *Inset graph* depicts vesiculation trends originating at X proceeding via growth only (G), growth plus nucleation ($G+N$), growth plus coalescence ($G+C$), coalescence only (C), and vesicle loss (L) with the *dashed arrows* representing the potential range between adjacent vesiculation processes. Our study indicates low V_G/V_L ratio and high $N_{V_{tot}}^m$ clasts most closely preserve the textures of melt at the time of fragmentation with further vesiculation processes proceeding in the fountain

1996), 2002 Stromboli lapilli (Lautze and Houghton 2007), and recent Strombolian and Hawaiian products from Etna (Polacci et al. 2009; Polacci et al. 2006). There is partial overlap in number density with 2004 products from Villarrica volcano (Gurioli et al. 2008) and the basaltic plinian eruption of Etna in 122 BC (Sable et al. 2006). The ranges of $N_{V_{tot}}^m$ for episodes 15 and 16 and episode 1 are nearly the same, though episode 15 contains more clasts with number densities $\sim 10^7 \text{ cm}^{-3}$.

Glass chemistry

Chemical analyses of glass in MLR versus MLF and MV versus LV zones (Fig. 6) of tephra from the late high-fountaining episodes of Kīlauea Iki are included in Table 2. MV and LV glasses are compositionally identical. Relative to the MLF zones, the matrix glass within MLR regions is slightly higher in TiO_2 and FeO and slightly lower in MgO and CaO .

Interpretation

Interpretation of macroscopic data

Deposits from episodes 15 and 16 have similar stratigraphy (Fig. 4a) and both are dominated by transitional material (Fig. 5a) but variations arise in the concentrations of other

clast types (Fig. 5a) and in the density distributions of clasts within samples (Fig. 4c). We interpret the transitional material with an oxidized core (T_O , Fig. 5e) as material from the cone that was observed tumbling back into the vent, where it mingled with melt and subsequently re-erupted as pyroclasts. After being erupted, some clasts (T_B , Fig. 5f, g) quenched on the exterior while the interior of the clast continued to expand, imparting a cracked, breadcrumb surface to the clasts. Some degree of expansion probably occurred within the fountain but must have also occurred after external surface quenching. This interior expansion, therefore, may have taken place either after clast exteriors were quenched in flight or, for the largest clasts, after deposition of clasts. Bomb-sized clasts are significantly larger than lapilli and take longer to quench completely (Tait et al. 1998).

In episode 15 (samples ρ_{11} , ρ_{09} , and ρ_{07} ; Fig. 4), minor variations in density (Fig. 4c) and componentry (Fig. 5a) correlate with the median grain size, maximum clast size, and increasing stratigraphic height (Fig. 4b). Density distributions for ρ_{11} and ρ_{09} (Fig. 4c) are similar, with a mean near 500 kg m^{-3} and correspond to the two coarsest intervals in episode 15 (Fig. 4b). Mean density shifts to slightly higher values at the end of the eruptive episode (sample ρ_{07} , 650 kg m^{-3}). As episode 15 progressed, there was a slight increase in abundance of both pumice and T_O clasts, the latter suggesting an increasing proportion of cone material failing and sliding into the vent.

The stratigraphic break at $\sim 43 \text{ cm}$ depth is inferred to represent the first material deposited during episode 16. Low spattering in the vent lasted only 20 min at the start of episode 16 before the fountain reached heights sufficient ($\sim 100 \text{ m}$) to result in deposition at the study site (Fig. 1). The volume of lava that drained back into the vent after episode 15 was ~ 3.2 million m^3 (Richter et al. 1970), some of which must have been cleared from the conduit during this first 20 min of low fountaining in episode 16. However, outgassed drained-back lake lava was probably still being expelled from the vent when high fountaining ensued. The fountain steadily increased from ~ 100 to 460 m in height over 25 min, producing the layer between 40 and 43 cm depth (Fig. 4a). Clasts from this stratigraphic level contain the greatest frequency of (80%) and largest (up to 1.5 cm diameter) MLR regions.

Episode 16 samples (ρ_{05} , ρ_{03} , and ρ_{01} ; Fig. 4) vary more than episode 15 in componentry, grain size, and density. The earlier-erupted samples, ρ_{05} and ρ_{03} , have mean densities of $\sim 700 \text{ kg m}^{-3}$ and correspond to grain size maxima. However, mean density increases to near $\sim 900 \text{ kg m}^{-3}$ and grain size decreases (Fig. 4b, c) at the close of this last high-fountaining phase of the entire eruption. Clasts in the last erupted sample include the full

Table 1 Vesicularity data for episode 15 and 16 clasts

Study	Density $\times 1,000$ (kg/m^{-3})	Density-derived ves% ^a	Crystal corrected ves% ^b	N_{Atot}^c (cm^{-2})	$N_{V\text{tot}}^d$ (cm^{-3})	$N_{V\text{tot}}^{m,e}$ (cm^{-3})
Kīlauea						
Kīlauea Iki Episode 15						
ρ09-P1	0.17	93.9	93.9	2.1E+03	2.4E+05	3.9E+06
ρ09-T10	0.33	88.2	88.8	6.7E+03	1.2E+06	1.1E+07
ρ07-T11	0.62	77.9	82.0	1.0E+04	2.0E+06	1.1E+07
ρ09-T9	0.53	81.1	81.1	1.3E+04	2.7E+06	1.4E+07
ρ07-F1	1.13	59.6	64.6	1.9E+04	6.4E+06	1.8E+07
ρ09-T42	1.11	60.4	62.5	1.5E+04	5.6E+06	1.5E+07
Kīlauea Iki Episode 16						
ρ05-P11	0.29	89.6	90.8	3.3E+03	5.6E+05	6.2E+06
ρ03-P2	0.27	90.4	90.4	2.7E+03	4.3E+05	4.5E+06
ρ01-P1	0.36	87.1	88.3	3.0E+03	8.1E+05	6.9E+06
ρ03-T20	0.32	88.6	89.2	4.0E+03	7.3E+05	6.7E+06
ρ05-T14	0.75	73.2	76.2	7.7E+03	2.0E+06	8.5E+06
ρ01-T19	0.94	66.4	71.2	9.6E+03	2.0E+06	6.9E+06
ρ03-T8	0.85	69.6	70.6	6.3E+03	2.0E+06	7.0E+06
ρ03-T59	1.15	58.9	59.5	1.5E+04	5.9E+06	1.5E+07
ρ05-T50	1.21	56.8	58.0	1.1E+04	3.9E+06	9.2E+06
Kīlauea Iki epi 1						
Chapter 4	0.34–1.5	50.0–87.9	53.8–87.9	2.6E+03–1.2E+04	6.3E+05–6.8E+06	3.8E+06–1.2E+07
Pū‘ū Ō‘ō						
Mangan and Cashman 1996		77–97			1.1E+02–1.8E+07	
Stromboli Lautze and Houghton 2007				7.1E+02–6.9E+03	9.3E+04–1.3E+06	1.9E+05–3.4E+06
Villarrica Gurioli et al. 2008	0.23–1.4	47.8–88.8		9.3E+02–8.5E+03	6.4E+04–2.1E+06	7.4E+05–1.4E+07
Etna						
<i>Hawaiian</i>				3.0–9.0E+02		
Polacci et al. 2009		52.0–81.0				
<i>Strombolian</i>				1.0–4.0E+02		
Polacci et al. 2009		52.0–73.2				
<i>Basaltic Plinian</i> Sable et al. 2006						2.6E+06–6.1E+07

^a Vesicularity calculated from density and DRE of $2,800 \text{ kg m}^{-3}$ computed using formula of (Bottinga and Weill 1970) based on known composition of episode 1 Kīlauea Iki lava (Richter et al. 1970)

^b Vesicularity calculated from density of clast minus percent density of olivine. Percent of olivine determined by amount of clast containing olivine in thin section

^c N_{Atot} values are the sum of bins from 0.005 to 40 mm

^d $N_{V\text{tot}}$ is the number of vesicles per unit volume of clast matrix, phenocrysts subtracted

^e $N_{V\text{tot}}^m$ is referenced to melt only, calculation based on phenocryst corrected (e) or $N_{V\text{tot}}$ -derived (f) vesicularity.

range of clast morphologies indicating a greater variety of thermal histories for individual clots of magma. At the close of the high fountaining, film footage shows the lava lake interacting with the fountain, resulting in large fluctuations in height and therefore, greater variety in residence times for clasts.

Interpretation of microscopic data

Similarities in clast vesicle data

Although clasts vary in vesicularity and morphology, they were all derived from the same parent magma (Table 2) and

Fig. 11 Number of vesicles (N) per equivalent diameter bin for episode 15 and 16 clasts. Low-vesicularity clasts represented by the *black line* contain the smallest vesicles of all clasts and intermediate- to high-vesicularity clasts contain the most abundant large vesicles

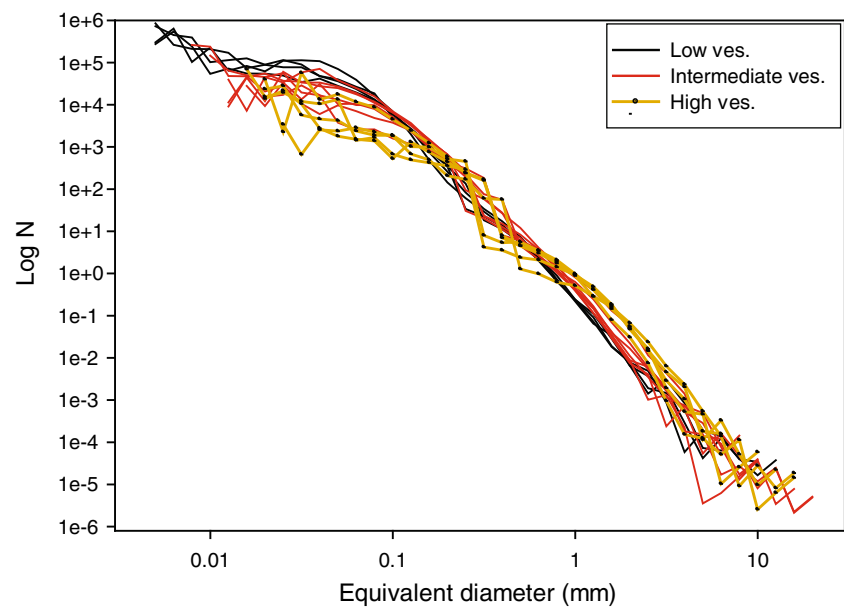


exhibit some common characteristics. Vesicle number densities (Fig. 10) span less than an order of magnitude (3.9×10^6 to 1.8×10^7 cm^{-3} ; Table 1), indicating similar history of bubble nucleation within the conduit. The dominance of spherical vesicles in all clasts suggests that most vesicles were able to relax back to spherical forms prior to quenching, although coalescence likely contributed to relatively larger vesicle sizes.

Variability in clasts across the range of vesicularity

Stovall et al. (2011) interpret high number densities and low vesicularities of fluidal clasts from episode 1 at Kīlauea Iki to indicate relatively rapid quenching that preserves a record of the vesiculation state of magma near the time of fragmentation. High vesicularity, pumiceous clasts (Fig. 5b) with fewer and larger bubbles underwent significant postfragmentation expansion, presumably in the thermally

insulated core of the fountain. Transitional clasts are interpreted as representing quenching at intermediate points along a postfragmentation path of growth and coalescence of bubbles within the interior of clasts in the fountain. The episodes 15 and 16 clasts follow similar trends on the number density versus V_G/V_L diagram (Fig. 10), and thus we infer a comparable interpretation applies to clasts in the episodes 15 and 16 deposits. The populations of smallest vesicles are in low-vesicularity clasts (Fig. 11), which we infer quenched before high-vesicularity clasts that lack small vesicles and contain relatively abundant larger-diameter vesicles. Pumice (Fig. 5b) forms the highest-vesicularity clasts (~85–93%) in the products of the 1959 eruption and are only slightly less vesicular than reticulite ($\geq 95\%$) from Pu‘u ‘Ō‘ō in 1983–86, inferred to have expanded within the core of Hawaiian fountains (Mangan and Cashman 1996; Stovall et al. 2011). Assuming these high-vesicularity clasts were fragmented with similar $N_{V_{\text{tot}}}^{\text{m}}$

Table 2 Chemical analysis of glass matrix in heterogeneous zones

Zone	MV $N=11^a$	LV $N=14^a$	ML free $N=12^a$	ML rich $N=10^a$	– Evolved ^b	+ Evolved ^b
SiO ₂	49.33 (0.26)	49.26 (0.33)	49.69 (0.34)	49.76 (0.39)	49.82	49.56
TiO ₂	2.75 (0.09)	2.76 (0.09)	2.73 (0.10)	3.00 (0.20)	2.89	3.00
Al ₂ O ₃	13.39 (0.07)	13.39 (0.09)	13.44 (0.14)	13.45 (0.21)	12.94	13.64
FeO	11.18 (0.13)	11.25 (0.12)	11.12 (0.20)	12.04 (0.54)	11.46	12.19
MnO	0.16 (0.03)	0.17 (0.02)	0.17 (0.02)	0.17 (0.03)	0.16	0.16
MgO	7.15 (0.07)	7.14 (0.08)	7.04 (0.31)	6.28 (0.55)	7.69	5.89
CaO	11.47 (0.07)	11.52 (0.08)	11.43 (0.07)	10.90 (0.51)	12.08	10.63
Na ₂ O	2.20 (0.07)	2.26 (0.03)	2.16 (0.11)	2.30 (0.09)	2.09	2.25
K ₂ O	0.56 (0.02)	0.56 (0.02)	0.56 (0.02)	0.68 (0.06)	0.54	0.67
P ₂ O ₅	0.28 (0.02)	0.28 (0.02)	0.28 (0.04)	0.32 (0.03)	0.28	0.33
Total	98.48	98.59	98.59	98.91	99.95	98.31

^a N =number of analyses and *italics numbers* are standard deviation

^bLess (–) evolved and more (+) evolved analyses represent extremes in the fractional crystallization trend within matrix glass of ML-rich zones

to low-vesicularity clasts, some coalescence must have occurred after fragmentation in the fountain (Stovall et al. 2011), producing lower $N_{V_{tot}}^m$ at the time of quenching (Fig. 10).

Interpretation of vesicle number densities

Vesicle number densities are, on average, lower in clasts from episode 16 than episode 15 (Fig. 9, 10, $N_{V_{tot}}^m$ in Table 1), and both are higher than episode 1 clasts. This assessment strengthens the argument that vesicle number density scales with intensity of activity (Polacci et al. 2006; Sable et al. 2006) since independent observations confirm that episode 15 produced the highest fountains.

Glass chemistry and microlite textures

Major element analyses of heterogeneous zones defined by contrasting vesicularity and lack or presence of microlites yield very similar glass compositions (Table 1). MV, LV, and MLF glass chemistries are identical and represent the same batch of magma. Additionally, these chemical analyses are strikingly similar to a robust study conducted on Kilauea Iki pumice by Helz (1987). Because the chemistry is identical in MV and LV zones, we cannot correlate these regions to two separate batches of magma with varying initial volatile contents. The variation in values between glass in MLR and MLF regions can be explained by crystallization of cognate plagioclase and pyroxene microlites.

The two distinctive microlite textures observed in episode 15 and 16 materials may be interpreted in the context of kinetic effects arising from variable cooling rates as explored in laboratory experimental studies. Dynamic cooling experiments on lunar picritic (Walker et al. 1976) and quartz normative basalt (Grove and Raudsepp 1978) indicate feldspar formation is dramatically suppressed relative to pyroxene at high cooling rate and less suppressed during slower cooling. As a consequence, rapid cooling causes pyroxene to crystallize alone over a large temperature interval, while slower-cooling causes pyroxene and plagioclase to co-crystallize and even intergrow to form fasciculate textures (Walker et al. 1978). Although the quantitative relationship between cooling rate and plagioclase suppression is dependent upon melt composition, the comparison is expected to provide a qualitative constraint on relative cooling rates experienced by the two textural types observed in episode 15 and 16 clasts.

In order to form fasciculate intergrowths of pyroxene and plagioclase microlites (Fig. 6c), MLR regions cooled slowly enough that pyroxene grew in combination with plagioclase due to limited supercooling and a reduced temperature separation between the two phases (Walker et al. 1978). We interpret this to have occurred in the lava

lake, where extended cooling times resulted in coprecipitation of both minerals. Lava lake material that drained back into the vent mingled with hot, previously unerupted, magma and was re-erupted during later fountaining. The incorporated lava lake material must have been still hot and fluid when mixed with conduit magma because blobs of melt from within MLR zones intruded into the adjacent MLF melt. Furthermore, to maintain similar vesicle textures between the two zones, drained-back melt must retain a largely unmodified vesicle population in addition to residual dissolved H₂O that can undergo further outgassing when re-erupted (Gerlach 1986).

Microlite stringers contain only dendritic or spherulitic pyroxene, which can be attributed to rapid cooling and crystallization relative to the slower-cooled MLR fasciculate textures. The dendritic pyroxene microlites along the edges of MLR zones indicate rapid crystallization relative to the interior and are likely to have formed when cooler MLR patches contacted and cooled the MLF melt, inducing pyroxene dendrite crystallization.

Discussion

Contrasts between extremely high (episodes 15 and 16) and high (episode 1) fountains

Variability in clast componentry and extent of postfragmentation expansion

There is a greater variety of clast types in deposits from episodes 15 and 16 than in those from episode 1 (Fig. 5). Episode 1 tephra has proportionally fewer pumice and more fluidal clasts indicating relatively rapid cooling times for these clasts. For episode 1, fountain heights never reached more than ~380 m and averaged near ~250 m for most of the episode. However, episodes 15 and 16 produced fountains that peaked at ~580 and ~460 m, respectively, and were sustained near 300 m height. Higher fountains yield a prolonged period of thermal insulation for clasts resulting in greater production of pumice in episodes 15 and 16. The higher fountains also transport larger clasts to higher elevations (Richter et al. 1970) where they become breadcrusted due to continued vesiculation in the interior of the bombs. Higher fountains and longer fountain residence times for episodes 15 and 16, even for the clasts located around the fountain perimeter, resulted in enhanced post-fragmentation vesiculation and few clasts with fluidal textures. The absence of T_O clasts in episode 1, and their occurrence in the latter episodes, is a simple consequence of the over-steepened geometry of the much larger late-stage cone, which resulted in frequent sliding of inner-wall material back into the vent to be re-erupted.

Variability in vesicle size for similar vesicularity clasts

In the highest fountaining episodes, the dominant vesicle size is smaller and V_G/V_L is larger. The lowest vesicularity clasts from episode 1 tephra have a dominant vesicle diameter of ~ 0.25 mm, whereas similar vesicularity clasts from episodes 15 and 16 tephra have vesicle size mode at 0.1 mm. To account for this difference, we propose that greater degrees of thermal insulation and therefore post-fragmentation expansion occur during the extremely high fountains.

Controls on extremely high fountaining behavior

To achieve the high fountain heights of the 1959 Kīlauea Iki eruption, the magma must have been erupted at great velocities. Fountain height increases with the mass fraction of exsolved volatiles (Polacci et al. 2009; Sparks et al. 1997) but can be limited by the degree of coupling between the gas and melt phases (Parfitt and Wilson 1995) or by the influence of an overlying lava lake (Wilson et al. 1995). VNDs for the Kīlauea Iki eruption are high and indicate sufficient exsolved volatiles to drive the observed fountains to sustained heights between 200 and 400 m (Richter et al. 1970). $N_{V_{tot}^m}$ for episode 1 is lower on average than for episodes 15 and 16 (Table 1). Overall, $N_{V_{tot}^m}$ values are highest for episode 15, the highest-fountaining episode of the eruption. Therefore, it appears that higher-fountaining episodes are associated with greater degrees of nucleation driving higher conduit ascent rates.

Conclusions

This study of the last two high-fountaining episodes of the 1959 eruption gives further evidence of the pervasiveness of postfragmentation processes occurring within Hawaiian fountains (Mangan and Cashman 1996; Stovall et al. 2011). Vesicularity correlates inversely with VND across both episodes (Fig. 10), which indicates that the number density of vesicles decreases as a result of an extended period of coalescence when erupted material experiences postfragmentation expansion within the fountain. Additionally, episode 15 and 16 clasts contain varying percentages of fasciculate-textured, microlite-rich inclusions, inferred to represent material recycled through the lava lake.

A question remains regarding the factors leading to termination of fountaining episodes at Kīlauea Iki and other Hawaiian eruptions. It has been assumed that encroachment of partially degassed lake lava into the vent at Kīlauea Iki added sufficient overpressure to the conduit to inhibit further vesiculation of magma (Eaton et al. 1987). Wilson et al. (1995) use parameters from the Kīlauea Iki eruption to

model the effect of vent-confining lava ponds on fountain height and determined that fountain height decreases as overlying pond depth increases. During Hawaiian activity, the fountain also entrains relatively outgassed, higher density lava as it erupts through the ponded material. Therefore, continued eruption and deepening of lava overlying the vent at Kīlauea Iki could have suppressed the fountain sufficiently so that gas exsolution from primary magma could no longer overcome the confining pressure imparted by the entrainment of increasing amounts of high-density material. However, this does not explain why cessation of fountaining in episodes 15 and 16, as well as in other episodes, occurred abruptly rather than gradually.

Based on this and the study of episode 1 tephra (Stovall et al. 2011), the relatively small and mechanically coupled vesicle population preserved in lapilli originates from late exsolution of volatiles, principally H_2O (Gerlach 1986; Wilson et al. 1995), which is the controlling factor for the rate of late-stage ascent and high fountaining. Assuming that exsolution of this gas phase occurred within the last ~ 120 m of the surface (Mangan and Cashman 1996), we must presume that another process transported the magma to this depth from the storage region.

Melt inclusions are found within olivine phenocrysts that formed in the upper part of Kīlauea's summit reservoir (Anderson and Brown 1993) shortly before erupting (Helz 1987). Analysis of these inclusions indicates that pre-eruptive bulk CO_2 contents of parental magma were near 0.22 wt.%, which provides sufficient buoyancy to the magma to rise into and mix with cooler, stored magma shallow in the Kīlauea summit-storage region (Anderson and Brown 1993). Eaton et al. (1987) suggest that between Kīlauea Iki fountaining stages, reservoir exsolution of CO_2 , and the resulting formation of a gas phase, would reduce the density of reservoir magma by 5–10% resulting in buoyant rise of gas-rich magma. Between fountaining stages, reservoir pressure was enhanced by the influx of volatile-rich magma from depth, the resulting formation of CO_2 -rich bubbles, and also by drainback of lava from the lake. If initial magma rise was most affected by the exsolution and decoupling of an earlier exsolved volatile species, it is possible that a stage of fountaining comes to an end when the supply of this gas is exhausted. However, excess pressure within the reservoir was also relieved as magma was erupted during each episode. At this stage, it is unclear which of these factors, or perhaps some combination of encroachment of lava into the vent, exhaustion of primary exsolved gas phase, or decrease in reservoir pressure, resulted in the termination of fountaining at Kīlauea Iki.

It has been proposed that, later in the eruption, enhanced reservoir pressure resulting from the combined drainback from the lake lava and continued influx of magma from

depth caused intrusion into the upper east rift zone (Eaton et al. 1987). As the Kīlauea Iki eruption proceeded and the reservoir pressure built, more lava was forced into the east rift zone (Eaton et al. 1987) during later stages of drainback. Presumably by the end of the final episode, this pathway was being utilized as the dominant magma passage away from the summit reservoir. The Kīlauea Iki conduit ceased to be utilized and the eruption ended. In mid-January, the east rift zone erupted at Kapoho.

Acknowledgments Special thanks to Carolyn Parcheta and Eric Hellebrand for help with microprobe operation; Maria Janebo for rock-wrapping assistance; Thomas Shea for creating FOAMS; and Gary Barnes, Ulrich Küppers, and Laura Pioli for reviewing this work. This research was funded by NSF grant EAR-0709303.

References

- Alparone S, Andronico D, Lodato L, Sgroi T (2003) Relationship between tremor and volcanic activity during the Southeast Crater eruption on Mount Etna in early 2000. *J Geophys Res* 108:2241–2254
- Anderson AT, Brown GG (1993) CO₂ contents and formation pressures of some Kilauean melt inclusions. *Am Miner* 78:794–803
- Andronico D, Cristaldi A, Scollo S (2008) The 4–5 September 2007 lava fountain at South-East Crater of Mt Etna, Italy. *J Volcanol Geotherm Res* 173:325–328
- Bertagnini A, Calvari S, Coltelli M, Landi P, Pompilio M, Scribano V (1990) The 1989 eruptive sequence. In: Barberi F, Bertagnini A, Landi P (eds). In: Mt. Etna: the 1989 eruption. Giardini: Pisa. pp 10–22
- Bottinga Y, Weill DF (1970) Densities of liquid silicate systems calculated from partial molar volumes of oxide components. *American Journal of Science* 269:169–182
- Eaton JP, Richter DH, Krivoy HL (1987) Cycling of magma between the summit reservoir and Kīlauea Iki lava lake during the 1959 eruption of Kīlauea volcano. In: Decker RW, Wright TL, Stauffer PH (eds). *Volcanism in Hawai‘i*. US Geol Surv Prof Pap, 1350: 1307–1334
- Gardner JE, Thomas RME, Jaupart C, Tait S (1996) Fragmentation of magma during Plinian volcanic eruptions. *Bull Volcanol* 58:144–162
- Gerlach TM (1986) Exsolution of H₂O, CO₂, and S during eruptive episodes at Kīlauea volcano, Hawai‘i. *J Geophys Res* 91:12177–12185
- Grove TL, Raudsepp M (1978) Effects of kinetics on the crystallization of quartz normative basalt 15597: an experimental study. *Proc Lunar Planet Sci Conf* 9:585–599
- Gurioli L, Harris AJL, Houghton BF, Polacci M, Ripepe M (2008) Textural and geophysical characterization of explosive basaltic activity at Villarrica volcano. *J Geophys Res* 113:B08206. doi:10.1029/2007JB005328
- Heliker C, Mattox TN (2003) The first two decades of the Pu‘u ‘Ō‘ō-Kupaianaha eruption: chronology and selected bibliography, The Pu‘u ‘Ō‘ō-Kupaianaha eruption of Kīlauea volcano, Hawai‘i: the first 20 years. US Geol Surv Prof Pap 1676:1–27
- Helz RT (1987) Diverse olivine types in the lava of the 1959 eruption of Kīlauea volcano and their bearing on eruption dynamics. In: Decker RW, Wright TL, Stauffer PH (eds), *Volcanism in Hawai‘i*. US Geol Surv Prof Pap, 1350: 1307–1334
- Houghton BF, Wilson CJN (1989) A vesicularity index for pyroclastic deposits. *Bull Volcanol* 51:451–462
- Lautze NC, Houghton BF (2007) Linking variable explosion style and magma textures during 2002 at Stromboli volcano, Italy. *Bull Volcanol* 69:445–460
- Mangan MT, Cashman KV (1996) The structure of basaltic scoria and reticulite and inferences for vesiculation, foam formation, and fragmentation in lava fountains. *J Volcanol Geotherm Res* 73:1–18
- Parfitt EA, Wilson L (1995) Explosive volcanic eruptions IX. The transition between Hawaiian-style lava fountaining and Strombolian explosive activity. *Geophys J Int* 121:226–232
- Polacci M, Corsaro RA, Andronico D (2006) Coupled textural and compositional characterization of basaltic scoria: insights into the transition from Strombolian to fire fountain activity at Mount Etna, Italy. *Geol* 3:201–204
- Polacci M, Burton MR, La Spina A, Mure R, Favretto S, Zanini F (2009) The role of syn-eruptive vesiculation on explosive basaltic activity at Mt. Etna, Italy. *J Volcanol Geotherm Res* 179:265–269
- Richter DH, Eaton JP, Murata KJ, Ault WU, Krivoy HL (1970) Chronological narrative of the 1959–60 eruption of Kīlauea volcano, Hawai‘i. In: The 1959–60 eruption of Kīlauea volcano, Hawai‘i. US Geol Surv Prof Pap, 537-E: E1–E73
- Sable JE, Houghton BF, Del Carlo P, Coltelli M (2006) Changing conditions of magma ascent and fragmentation during the Etna 122 BC basaltic Plinian eruption: Evidence from clast micro-textures. *J Volcanol Geotherm Res* 158:333–354
- Shea T, Houghton BF, Gurioli L, Cashman KV, Hammer JE, Hobden BJ (2009) Textural studies of vesicles in volcanic rocks: an integrated methodology. *J Volcanol Geotherm Res* 190:271–289
- Sparks RSJ, Burski MI, Carey SN, Gilbert JS, Glaze LS, Sigurdsson H, Woods AW (1997) *Volcanic plumes*. Wiley, Chichester
- Stovall WS, Houghton BF, Gonnermann HM, Fagents SA, Swanson DA (2011) Eruption dynamics of Hawaiian-style fountains: the case study of episode 1 of the Kīlauea Iki 1959 eruption. *Bull Volcanol* 73:511–529. doi:10.1007/s00445-010-0426-z
- Swanson DA, Duffield WA, Jackson DB, Peterson DW (1979) Chronological narrative of the 1969–71 Mauna Ulu eruption of Kīlauea volcano, Hawai‘i. US Geol Surv Prof Pap 1056:1–55
- Tait S, Jaupart C, Thomas R, Gardner J (1998) Constraints on cooling rates and permeabilities of pumice in an explosive eruption jet from colour and magnetic mineralogy. *J Volcanol Geotherm Res* 86:79–91
- Walker GPL, Croasdale R (1972) Characteristics of some basaltic pyroclastics. *Bull Volcanol* 35:303–317
- Walker D, Kirkpatrick RJ, Longhi J, Hays JF (1976) Crystallization history of lunar picritic basalt sample 12002: phase-equilibria and cooling-rate studies. *Geol Soc Am Bull* 87:646–656
- Walker D, Powell MA, Lofgren GE, Hays JF (1978) Dynamic crystallization of a eucrite basalt. *Proc Lunar Planet Sci Conf* 9:1369–1391
- Wilson L, Parfitt EA, Head JW (1995) Explosive volcanic eruptions VIII. The role of magma recycling in controlling the behaviour of Hawaiian-style lava fountains. *Geophys J Int* 121:215–225